stellarator news

Published by Fusion Energy Division, Oak Ridge National Laboratory
Building 5700 P.O. Box 2008 Oak Ridge, TN 37831-6169, USA

Editor: James A. Rome Issue 120 June 2009
E-Mail: jar@ornl.gov Phone (865) 482-5643

On the Web at http://www.ornl.gov/sci/fed/stelnews

Photogrammetric survey of magnetic field lines in the stellarator WEGA

Introduction

The confinement quality of the magnetic field in a stellarator is generally very sensitive to field errors, e.g., deviations in the position and orientation as well as the shape of the magnet coils. It is therefore necessary to characterize the magnetic configuration and prove the existence of closed and nested flux surfaces. Since the vacuum field in a stellarator—produced only by the external coils—is already confining, this check for field integrity can be done experimentally without plasma. A common method [1, 2] of surveying the field structure utilizes an electron beam, which follows the field line due to reduced perpendicular mobility. A fluorescent mesh or a moving fluorescent bar is necessary to detect the intersection points of the beam in a poloidal cross section. So far, only the detection principle limits the measured data to a two-dimensional cut view. The electron beam trajectory follows the whole field line on its flux surface, so that an alternative beam measurement technique can offer spatial information. Using a background gas, it is possible to visualize the beam via electron-impact excitation of the gas particles [3]. This luminescent trace is visible throughout the stellarator and can be observed from different viewpoints and measured by means of photogrammetry. The trace is limited in range due to a finite initial energy of the electrons and a steady energy loss in the excitation processes. This less invasive technique, which provides a three-dimensional (3D) measurement of the magnetic field lines, was applied and optimized at the WEGA stellarator at Max-Planck-Institut für Plasmaphysik, Greifswald.

The experimental setup

The experiment WEGA is a classical stellarator with a major radius $R_0 = 72$ cm and a minor radius $r_0 = 19$ cm for the toroidal plasma vessel. Forty toroidal and two helical copper coils produce a magnetic field $B_0 = 50–600$ mT with a rotational transform $\iota\!\!-= \iota/2\pi = 0.1, \ldots, 1$ for a typical flat-top time of $t_M = 30$ s. A more detailed description of the stellarator WEGA can be found in [4].

The free electrons for the beam were provided by a heated tungsten wire and accelerated to an initial energy $E_0 = e \cdot U_A$ with the acceleration voltage U_A applied between the wire (cathode) and metal cup (anode) with a hole. The vessel was at the same potential as the anode to screen the electric field outside the electron gun. Figure 1 shows the measurement setup at the stellarator using four viewpoints with overlapping fields of view. Inside the vessel, which was evacuated to a pressure p between 10^{-3} and 10^{-6}

In this issue . . .

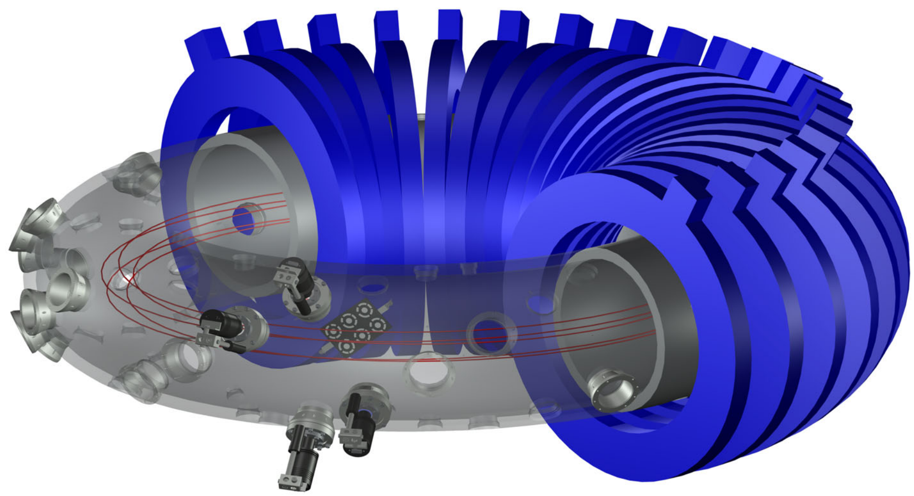

Fig. 1. Experimental setup with toroidal field coils (dark blue), vacuum vessel (grey), luminescent trace of the electron beam (red), four observation cameras (black) and six reference marks mounted on the high field side (white dots with rings).

mbar, a set of reference marks was installed to determine the exact camera positions. The pictures were taken by a Starlight Express^{TM} HX916 monochrome camera using a Peltier-cooled CCD chip with a resolution of 1300 × 1030 pixels, allowing detailed images and long exposures of up to $t_E = 5$ s. To retrieve the 3D coordinates of the visible trace, the commercial photogrammetry software AICON 3D-Studio [5] was used. The program calculates the light ray going from the visualized field line through the optical system to the pixel on the image sensor with a ray tracing algorithm. By taking two different pictures from the same section of the field line transition, the intersection points of the respective calculated light rays provide the coordinates of the measured trace. The precise optical and geometric properties of the lens system and image sensor were checked in a prior calibration. In addition, the exact locations and orientation of the cameras were determined using a calibrated set of reference points visible in the background of every image.

Results

The electron beam was optimized for high luminescence, long range, and small divergence. The main dependences occurred for different gas pressures p, gas types, field strengths B_0, and acceleration voltages U_A. The effect of these parameters on the range of the visible trace was additionally compared with a collision model taking into account inelastic and elastic scattering of electrons, atoms, and ions. Although qualitative agreement was found, charge accumulation, space charge effects, and increases in pitch angle seemed to be non-negligible but unconsidered factors.

Regarding the electron gun, the shape and design of the anode had a strong influence on both the emission current and the distribution of electrons with different pitch angles in the beam.

For application at WEGA, the range of the visible trace was not maximized but limited to ensure easy distinction of the different revolutions. As a result, photos like that in Fig. 2 were taken for a magnetic configuration with $\iota \approx 0.2$ at $B_0 \approx 589$ mT. Argon served as background gas at $p \approx 4 \times 10^{-4}$ mbar. The emitted electrons with a current of $I_E \approx 2$ mA had an initial energy of $E_0 \approx 300$ eV. Thus, the beam created a visible trace of 5 revolutions or $s \approx 24$ m in length and a beam cross-section diameter $d \approx 5$ mm.

As shown in Fig. 2, photos of the luminescent traces and the reference points have been taken sequentially and merged via photo editing to handle the high contrast between reference points, traces and background. These perspective pictures from four angles of view were processed by the photogrammetry software, and a measured point cloud of the trace was obtained.

It was possible to measure up to the fourth revolution of one magnetic field line in the stellarator with an accuracy of about ±5 mm. By measuring part of the fourth revolution, this is equivalent to a sensitivity in the rotational transform of $\Delta\iota = 0.004$. The sketches in Fig. 3 show a comparison between the measured points and a numerical simulation [6] of a drift path of equivalent electrons. As can be seen, the trajectories are not exactly the same; rather, they are shifted and tilted. This produces an additional deviation up to $\Delta r = 7$ mm at the fourth revolution. This deviation results from the determination of the camera positions using inaccurate positions of the reference marks and problems with merging the sequential photos.

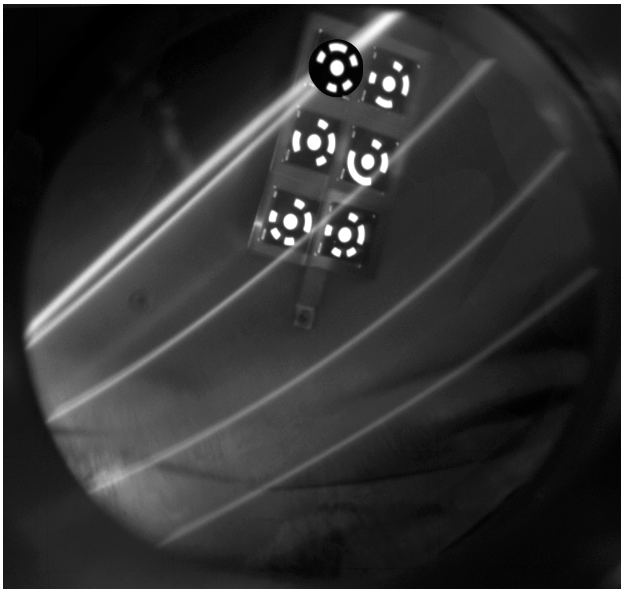

Fig. 2. Photo of one visualized magnetic field line with five transitions in the field of view and six reference marks inside the torus.

Outlook

The proof of principle for this 3D measurement technique for magnetic field lines was given, although some work on improving the accuracy remains to be done. In particular, better camera position determination by using a more accurate mount for the reference marks would be beneficial. In order to prevent unintended interaction with the plasma in later experiments, it would also be preferable to use distinct features of the plasma vessel as reference points rather than additional marks mounted on a carrier.

Nevertheless, this technique presents an alternative way of characterizing vacuum stellarator fields, and its use for the first magnetic field tests at Wendelstein W7-X is under discussion. Additional fields of application are the alignment and adjustment of toroidally separated plasma diagnostics aimed at specific parts of the magnetic field, such as the magnetic axis or the last closed flux surface. Furthermore, this principle could be used for an experimental 3D investigation of trapped particle orbits, with an appropriate electron gun that emits particles with a high fraction of the impulse perpendicular to the magnetic field line.

P. Drewelow, M. Otte, T. Bräuer, and F. Wagner
Max-Planck-Institut für Plasmaphysik
Greifswald Branch
17491 Greifswald, Germany
E-mail: drewelow@physik.hu-berlin.de

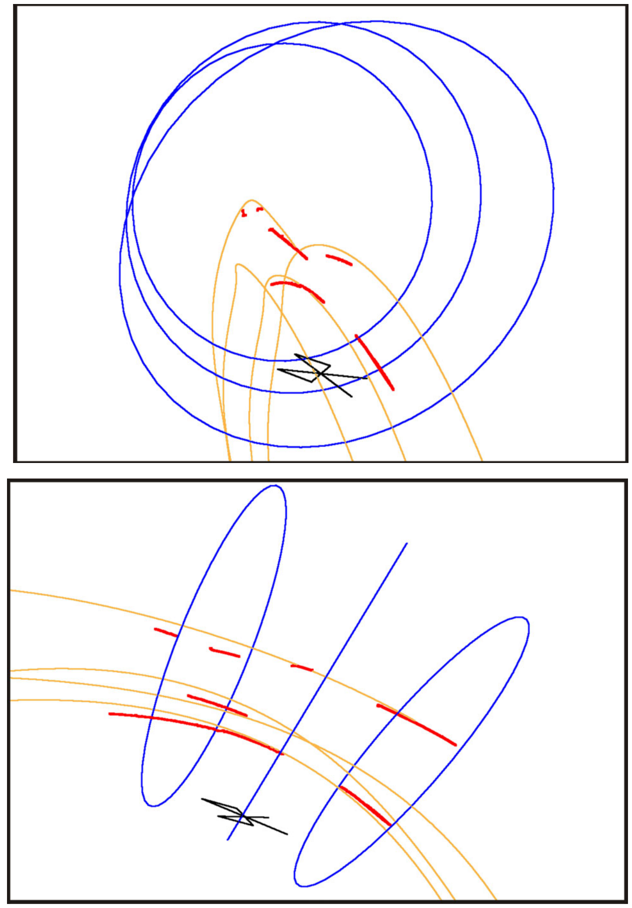

Fig. 3. Comparison of measured data (red) with numerically calculated drift trajectories (orange) viewed from above (top) and inside (bottom) on the plasma vessel (dark blue contours). The black figure represents the six connected reference marks.

References

[1] M. Otte and J. Lingertat, "Initial Results of Magnetic Surface Mapping in the WEGA Stellarator," Proc. 29th EPS Conf. Plasma Phys. Contr. Fusion, Montreux, 17–21 June 2002, ECA, Vol. 26B, p. 5.036 (2002).

[2] M. Otte et al., "Magnetic Flux Surface Measurements at Wendelstein W7-AS," *Stellarator News* 100, p. 2–5 (2005).

[3] O. Neubauer, F. H. Bohn et al, "Measurement of the Vertical Magnetic Field in TEXTOR using the Electron Beam Technique," Fusion Sci. Technol. **31**, 154–158 (1997).

[4] M. Otte et al., "The WEGA Stellarator: Results and Prospects," AIP Conf. Proc. **993**, 3–10 (2008.

[5] AICON 3D Studio, AICON 3D Systems GmbH, www.aicon.de.

[6] A. Werner, Max-Planck-Institut für Plasmaphysik, Greifswald, private communication.

Electron cyclotron emission from the WEGA stellarator

After installation of the new 28-GHz electron cyclotron resonance heating (ECRH) system (gyrotron) at the stellarator WEGA (Max-Planck-Institut für Plasmaphysik, Greifswald) electron temperatures clearly exceeding 15 eV are expected [1]. In this paper we describe the recently installed electron cyclotron emission (ECE) diagnostic. Because ECE is the standard temperature diagnostic in fusion research, it should be tested at WEGA. The first tests presented here have been carried out using a 2.45-GHz ECRH system with electron temperatures of about 5 eV. Under these conditions the emission is dominated by bremsstrahlung; however, the existence of ECE has been demonstrated.

WEGA is a medium-sized classical $\ell = 2$, $m = 5$ stellarator with major radius $R \approx 72$ cm and maximum plasma radius $a \approx 11$ cm. For central power deposition in the plasma using the 10-kW, 28-GHz ECRH system, the magnetic flux density on the plasma axis must be $B_0 = 0.5$ T to be resonant at the second harmonic of the electron cyclotron frequency. In addition to this resonant case, the plasma can be heated non-resonantly at $B_0 = 0.5$ T by the 2.45-GHz system (26 kW). Nearly the same electron densities up to $n_e = 5 \times 10^{18}$ m^{-3} with typical electron temperatures T_e = 5 eV can be reached in both cases.

To calculate the total expected microwave emission of the plasma, an integration of the emission coefficient along the sight line must also include absorption. In the case of high optical depth ($\tau \gg 1$), line integration of the local absorption coefficient along the propagation direction of the electromagnetic wave leads to a direct proportionality of observed intensity to T_e. The second harmonic of the perpendicularly polarized wave (X2-mode) has the highest optical depth and is generally used for temperature diagnostic [2]. The optically thin plasmas at WEGA have $\tau <$ 0.1 in the expected X2 frequency range from 25 GHz to 35 GHz, so that wall reflections at the metallic walls of the torus have to be considered. This leads to an observed radiation temperature $T_s = T_e(1 - e^{-\tau})/(1 - \Gamma e^{-\tau})$ with a typical value of $T_s = 0.1 T_e$ for a reflection coefficient $\Gamma > 0.9$.

To detect the microwave radiation emitted by the plasma, a multichannel radiometer system was installed (Fig. 1).

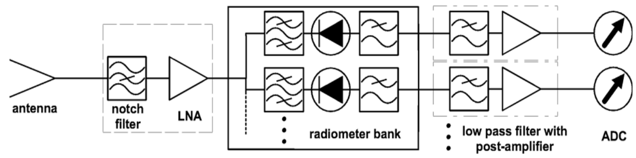

Fig. 1. Block diagram of the ECE diagnostic.

The radiation is received by a horn antenna and preamplified by a low-noise-amplifier (LNA) with a noise temperature of 230 K and 22 dB gain. Conversion to a lower frequency band by a heterodyne technique is not necessary due to the availability of amplifiers in the frequency range up to 40 GHz [2]. The signal is split by means of power dividers and bandpass filters into 12 frequency bands. The power of the incident radiation is measured using incoherent detectors. The radiometer filter bank could be taken from the earlier ECE system of Wendelstein 7-AS (W7-AS) [3]. Of the existing 12 channels, 7 are within the expected electron cyclotron frequency range on WEGA. To protect the sensitive preamplifier against the strong 28-GHz radiation of the gyrotron, a notch filter based upon lateral coupling of cavity resonators at a waveguide was built. The H_{011} mode was selected as the induced wave field at 28 GHz. Figure 2 shows the transmission characteristic of the notch filter using four serial connected resonators.

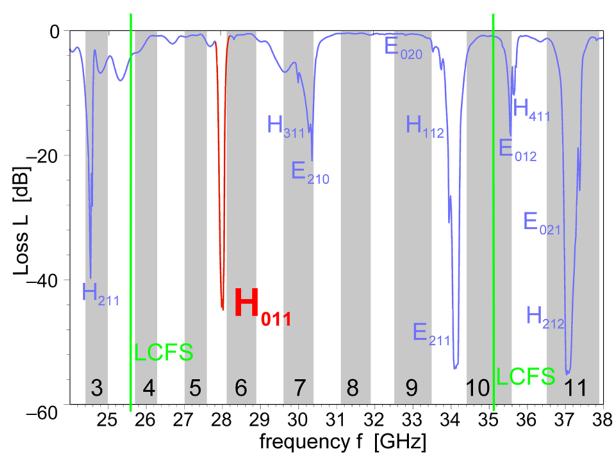

Fig. 2. Notch filter loss *L* versus frequency *f*. Grey shaded frequency ranges show bandpass filters of the radiometer channels. The H_{011} main resonance at 28 GHz induces suppression up to 45 dB.

The vertical green lines indicate the region of expected ECE at second harmonic according to the plasma area within the last closed flux surface (LCFS), see Fig. 3 for orientation.

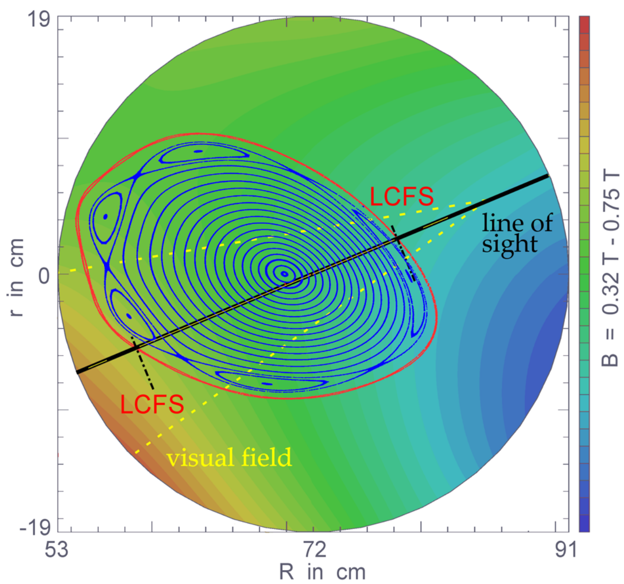

Fig. 3. Pointier plot of a WEGA configuration with $\iota_a = 1/5$ and the magnitude of magnetic flux density color coded in the background.

An overlap of different harmonics does not exist. The filter was designed in such a way that the sensitivity of channels covering the ECE frequency range is only weakly affected by parasitic resonances. The sensitivity of the channels was determined with the aid of a hot-cold technique [2] using blackbody radiation at room temperature and liquid nitrogen. The measured values are in the region of
30 μV/K.

The first measurements with the new microwave diagnostic investigated plasmas using nonresonant heating at 2.45 GHz and 0.5 T and demonstrated the performance of the whole ECE system. Evidence for cyclotron emission was found in a specially designed discharge scenario shown in Fig. 4 where two time windows with different magnetic field are compared.

The magnetic flux density was chosen such that the ECE X2 emission is once outside the detection range of the radiometer ($B_0 = 0.35$ T, $f_{c,X2} = 19.6$ GHz) whereas the ECE shifts towards the central frequency channels for the higher field ($B_0 = 0.49$ T, $f_{c,X2} = 27.5$ GHz). To guarantee a constant radiation level, the heating power P_{out} was adjusted at 0.49 T such that the line-integrated density ndl was kept constant. The agreement of electron density n_e and electron temperature T_e profiles was checked with Langmuir probes. The bottom time trace shows as an example the corresponding radiation temperature of the channel with a mid-frequency of 31.5 GHz. The measured value correlates with the line-integrated density and the magnetic flux density. It also makes clear that the system has the ability to detect radiation temperature values downward to 0.1 eV. For better comparability Fig. 5 depicts the radiation temperature vs time and the mid-frequency of the channels.

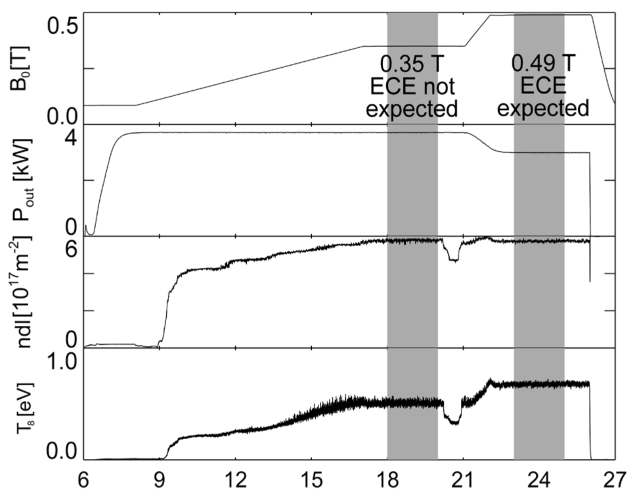

Fig. 4. Time traces of magnetic flux density B_0 on the axis, heating power P_{out}, line-integrated density n dl, and radiation temperature T_S.

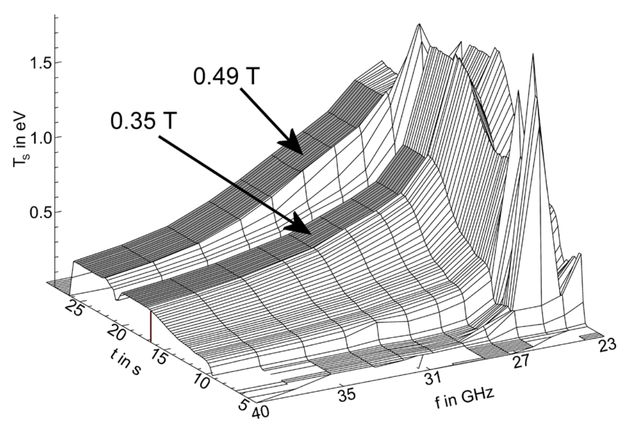

Fig. 5. Radiation temperature T_S vs time t and mid-frequency f of the radiometer channels.

A monotonic decrease of the radiation temperature with higher frequency is obvious. With step-up of the magnetic flux density from 0.35 T to 0.49 T, the radiation temperature in the channels with additionally expected ECE increases, too. Before this rise can be identified as cyclotron emission, the source of the emission for magnetic field values up to 0.35 T must be clarified. A third harmonic in this amplitude would demand an increase of emission in the two channels above 37 GHz at the magnetic field of 0.49 T. Taking into account that low-temperature plasmas are dominated by collisions, bremsstrahlung also has to be considered. The integrated value of the emission coefficient of bremsstrahlung and cyclotron radiation is in the same order of magnitude but the typical exponential decay of bremsstrahlung with frequency is not expected in the microwave range. However, applying a simple one-dimensional radiative transfer model results in a similar frequency dependency of their expected radiation temperature [4]. Figure 6 shows the radiation temperature vs the frequency at a magnetic flux density of 0.35 T.

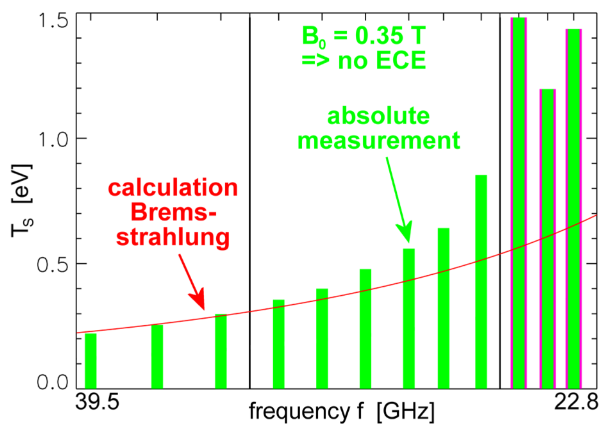

Fig. 6. Radiation temperature T_S vs mid-frequency f of the radiometer channels at a magnetic flux density of 0.35 T.

The vertical black lines indicate the frequency range with expected cyclotron emission at a magnetic flux density of 0.49 T. ECE is expected only in the channels outlined in red. The red curve shows the calculated radiation temperature of bremsstrahlung, taking wall reflections based on this simple model into account, confirming the observed magnitude as well as the basic frequency dependence. However, to make a unique identification of the observed jump in the radiation temperature with ECE, a reference field larger than 0.35 T is necessary so that the reference case channels with expected ECE fall in the frequency range of the diagnostic. This is used for Fig. 7, which plots the increase of the radiation temperature at 0.49 T with respect to two different reference fields.

The overlapping channels are outlined in red. At both reference fields (0.40 T and 0.44 T), these channels are separated by an edge from the other ones. This observation shows ECE as an additional radiation process. Hence a mixing of two different radiation processes is reflected in this temperature range. At electron temperatures above 15 eV the possibility of their quantitative determination via ECE is expected. However, considering the wavelength and plasma dimensions a full-wave calculation is additionally necessary for this purpose.

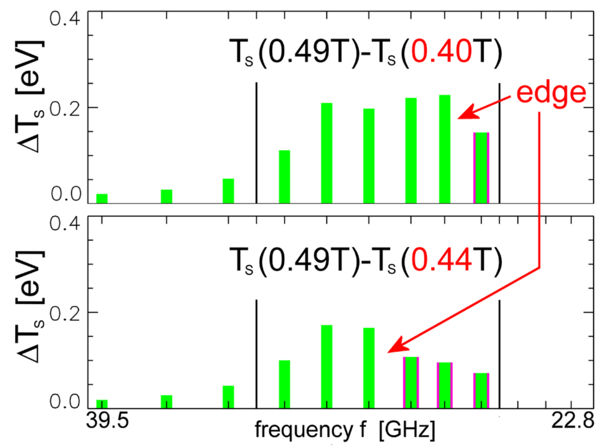

Fig. 7. Difference of radiation temperatures T_S at magnetic flux density of 0.49 T and chosen reference field versus mid-frequency f of channels.

Acknowledgement

The authors are grateful to Thomas Geist, Friedrich Wagner, and Heinrich Laqua for their contributions to the experiment and thank Dieter Aßmus and Ralf Gerhardt for their technical support.

T. Stange, H.-J. Hartfuß, M. Hirsch, M. Otte, S. Marsen, and S. Schmuck
Max-Planck-Institut für Plasmaphysik
Greifswald Branch, EURATOM Association
17491 Greifswald, Germany
E-mail: torsten.stange@ipp.mpg.de

References

[1] H. P. Laqua, D. Andruczyk, E. Holzhauer, S. Marsen, M. Otte, Y. Y. Podoba, J. Preinhealter, J. Urban, and G. B. Warr, "Electron Cyclotron Wave Experiments at the WEGA Stellarator," Proc 34. EPS Conf. Plasma Phys., Warsaw 2007, European Conf. Abstracts **31F** P-1.154 (2007).

[2] H. J. Hartfuß, T. Geist, and M. Hirsch, "Heterodyne methods in millimetre wave plasma diagnostics with applications to ECE, interferometry and reflectometry," Plasma Phys. Control. Fusion **39,** 1693–1769 (1997).

[3] Ch. Fuchs and H. J. Hartfuß, "Technology of the new W7-AS broadband radiometer system," Fusion Eng. Des. **53,** 451–456 (2001).

[4] G. Bekefi, Radiation Processes in Plasmas, John Wiley and Sons, Inc., New York, London, Sydney (1966).

Electrostatic potential measurement using a 6-MeV heavy ion beam probe in LHD

Introduction

A heavy ion beam probe (HIBP) is a unique diagnostic tool to measure the electrostatic potential, together with the potential and density fluctuations, directly and simultaneously in high-temperature magnetically confined plasmas. In nonaxisymmetric plasmas, the radial electric field is a key parameter for both neoclassical transport and anomalous transport.

In the Large Helical Device (LHD) at Toki, Japan, an HIBP has been in development since the beginning of the project. Recently, potential profiles and fluctuations have been observed using the HIBP [1, 2]. Here the HIBP system is described and some observations using the HIBP are reported.

HIBP system on LHD

In an HIBP, singly charged positive ions are injected into a plasma as a primary beam, and doubly charged ions obtained by ionization due to collision with the plasma on the path of this beam are detected (referred to as the secondary beam). In order to extract the probe beam from the plasma, the Larmor radius of the probe beam must be comparable with the size of the plasma device. Since the magnetic field in LHD is up to 3 T and the device size is a few meters, singly charged heavy ions with energies of several million electron volts are required for the primary beam. To date, the highest energy achieved has been 2 MeV for the HIBP in the TEXT-U tokamak, in which some technical difficulties were experienced in high-voltage operation. In order to reduce difficulties, a tandem accelerator and a new type of energy analyzer have been adopted in the LHD HIBP.

Unlike previous HIBPs, a tandem accelerator is used in the LHD HIBP to reduce the acceleration voltage. A tandem accelerator has an ionizer, which is a gas cell for the LHD HIBP, at the center, and high positive voltage is applied there. Singly charged negative ions, which are Au^- for the LHD HIBP, are initially injected into the accelerator and accelerated towards the gas cell. They are ionized positively (Au^+, Au^{2+}, …) by collisions with neutral particles in the gas cell. Then, they are accelerated again toward the other side port, which is grounded. Thus, the tandem accelerator can accelerate the beam particles twice, and only half of the acceleration voltage corresponding to the required energy of a singly charged positive ion beam is required. On the other hand, the tandem accelerator requires negative ions for the initial beam. From the point of view of ion mass and reliability as a negative ion source, gold ions (Au^-) were selected and have been developed for the LHD HIBP. The singly charged positive ions (Au^+) which are accelerated and extracted from the accelerator are injected into plasmas. A beam energy of 6 MeV is needed to measure the potential using the Au^+ beam at the magnetic axis with a magnetic field strength of 3 T, so the maximum acceleration voltage of the tandem accelerator is 3 MV.

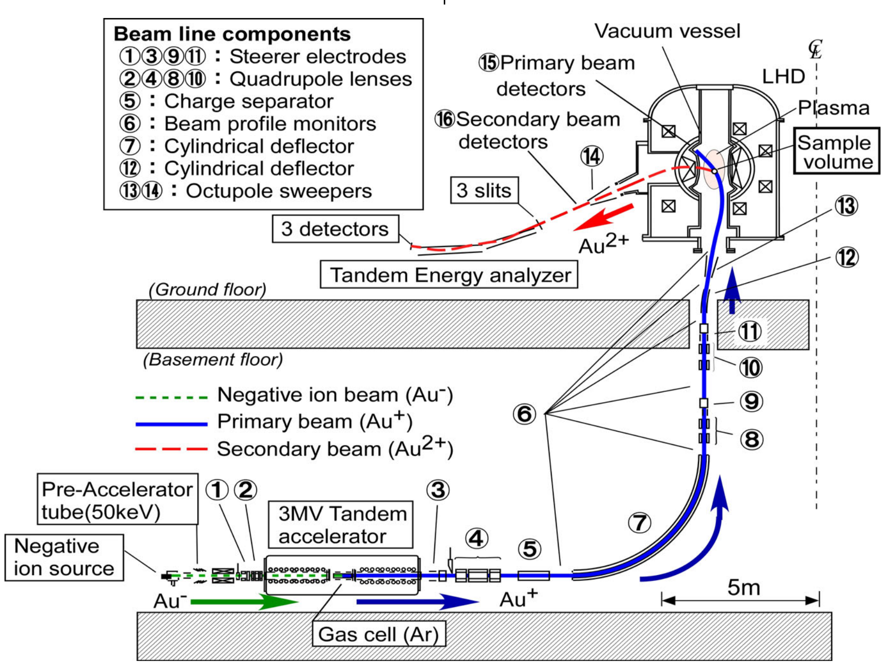

Fig. 1. Schematic view of the LHD HIBP.

The probe beam is injected through the bottom port of the LHD vacuum vessel, and the secondary beam obtained by ionization due to collision with the plasma is selected and detected at the horizontal port. Octupole deflectors are installed at the injection and detection ports, and both are used to control the beam trajectory in three dimensions. This "active trajectory control" method was developed for an HIBP in the Compact Helical System (CHS). The geometry of the LHD HIBP is shown in Fig. 1.

The variation in beam energy, which corresponds to the electrostatic potential at the ionization position of the probe beam, must be analyzed. Parallel-plate electrostatic analyzers are usually used for HIBPs because they have the desirable property of second-order focusing for the incident angle. However, this type of analyzer requires an impractical voltage of several hundred kilovolts for the MeV-range beam of the LHD HIBP. Hence, we have devised a new energy analyzer with two sets of electrodes: a tandem parallel-plate energy analyzer. The incident angles of the tandem energy analyzer are designed as 6 degrees for the first electrode and 10 degrees for the second electrode, in contrast to the 30 degrees of a conventional parallel-plate analyzer. Consequently, the required voltages can be reduced to 56.5 kV on the first electrode and 113.6 kV on the second electrode for a 6-MeV beam, and this new analyzer has been verified to work successfully in the LHD HIBP system.

The observable area is shown in Fig. 2. The potential profile can now be measured in the core region by the HIBP. Since the radial electric field E_r in the edge region can be measured using charge-exchange spectroscopy (CXS) in LHD, the E_r profile in the whole region can be measured with the HIBP and CXS. Complementary measurements using both the HIBP and CXS will advance the study of the physics of radial electric field formation in helical plasmas.

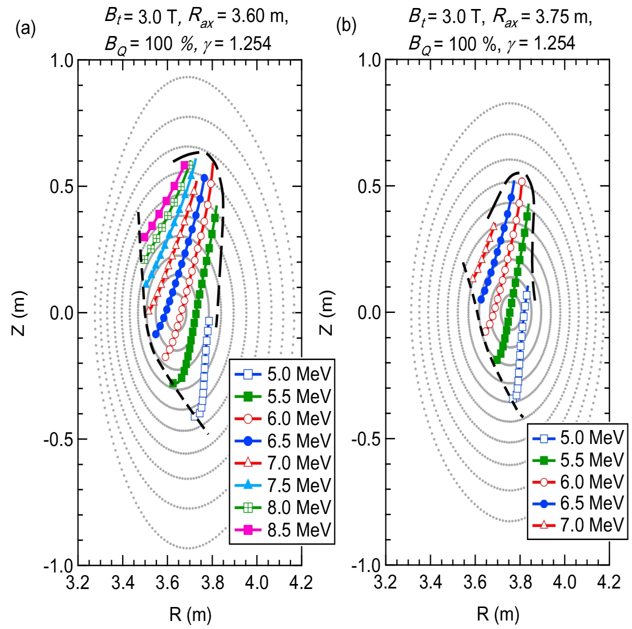

Fig. 2. Observable region. (a) R_{ax} = 3.6 m, B_Q = 100%, γ = 1.254. (b) R_{ax} = 3.75 m, B_Q = 100%, γ = 1.254. The beam energy is shown in the legend in each figure. The sample volume traces the marked curve during a sweep of the probe beam. The sample volume of the probe beam with the same Larmor radius ($L_b \propto \sqrt{E_b}/B_t$) traces the same curve, where E_b and B_t are the beam energy and the toroidal magnetic field strength, respectively.

Potential profile and fluctuation measurement

In this section, as an example of potential measurement by the HIBP, the change in the potential profile during electron heating and the characteristic potential fluctuations in plasmas with weak magnetic shear are shown.

In LHD, the rotational transform is controlled by use of electron cyclotron current drive (ECCD) [3]. Weak or negative magnetic shear profiles are formed during ECCD in the co-direction, which increases the rotational transform in the core region, and then characteristic magnetic and electrostatic fluctuations are observed.

The plasma is produced and sustained by balanced tangential neutral beam injection (NBI), and the line-averaged electron density is 0.1×10^{19} m^{-3} and constant. ECCD is superposed for 0.6 s, and weak magnetic shear profiles are formed by ECCD as shown in Ref. [3]. The electron temperature and electrostatic potential profiles during and after ECCD are shown in Fig. 3. A positive electric field is formed in the core region during ECCD because of the electron heating, and the transition to the electron root predicted by neoclassical theory qualitatively accounts for this behavior of the potential profiles.

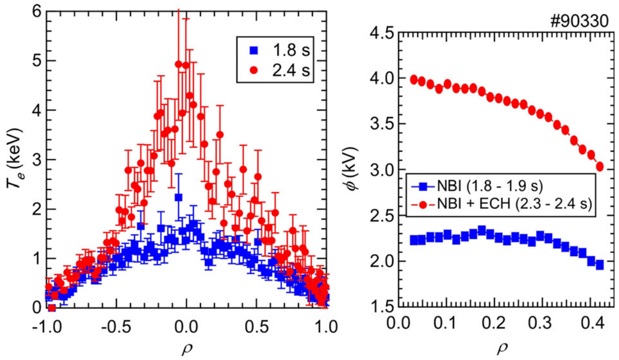

Fig. 3. (a) Electron temperature profiles and (b) electrostatic potential profiles. The plasma is produced and sustained by balanced tangential NBI, and ECCD is superposed from 1.3 to 1.9 s. The reference electrostatic potential is on the LHD vacuum vessel.

During ECCD, several magnetic fluctuations are observed at frequencies ≥ 40 kHz, and their frequencies change gradually with a time constant of a few hundred milliseconds as shown in Fig. 4(a), though the electron temperature and density are constant. The frequency shift seems to reflect a change in the rotational transform profile. Similar fluctuations are observed in plasmas with weak or reversed magnetic shear produced by neutral beam current drive (NBCD) [4], and the fluctuations are the reversed-shear-induced Alfvén eigenmodes (RSAEs).

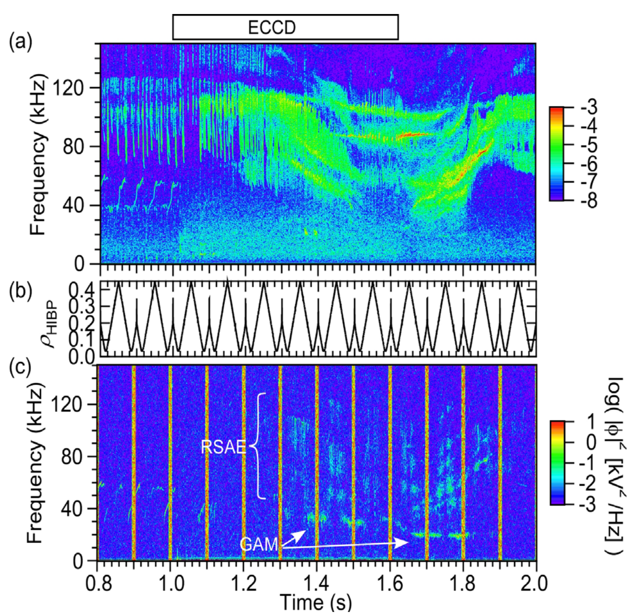

Fig. 4. (a) Spectrogram of the magnetic fluctuation. (b) Measurement position of the HIBP. (c) Spectrogram of the electrostatic potential fluctuation.

Fluctuations are also observed in the potential spectrogram measured using the HIBP, where the measurement position of the HIBP is reciprocated from ρ ~ 0.1 to ρ ~ 0.4 at a frequency of 10 Hz (Fig. 4(b)) and the spectrogram includes not only the temporal evolution but also the spatial structure. As shown in Fig. 4(c), several modes whose frequencies vary in the frequency range of 40 kHz and more in the potential fluctuation are observed, as in the magnetic fluctuation. In addition to that, a potential fluctuation with a constant frequency of about 35 kHz during ECCD and 20 kHz just after ECCD is observed. The frequency depends on the square root of the electron temperature, and its absolute value almost agrees with the geodesic acoustic mode (GAM) frequency. The mode is not observed in plasmas without tangential NBI. Thus, the mode with the constant frequency will be the energetic particle-induced GAM.

As mentioned above, since the spectrogram shown in Fig. 4(c) includes information about the spatial structure as well as the temporal evolution, the spatial distribution of the potential fluctuations can be estimated. Figure 5 shows the distribution of the power of each mode [5]. The lower frequency mode exists in inner region, and the mode with the GAM frequency is excited in the innermost region.

At present, the mode structure is not identified. A multichannel detector, which is under development, will help us clarify more precise structure of the potential profile and fluctuation.

From the point of view of turbulence measurement, the signal-to-noise ratio is not sufficient to detect the turbulent potential fluctuation. The development of a high-power negative ion source and more efficient detector is necessary, and it is under way.

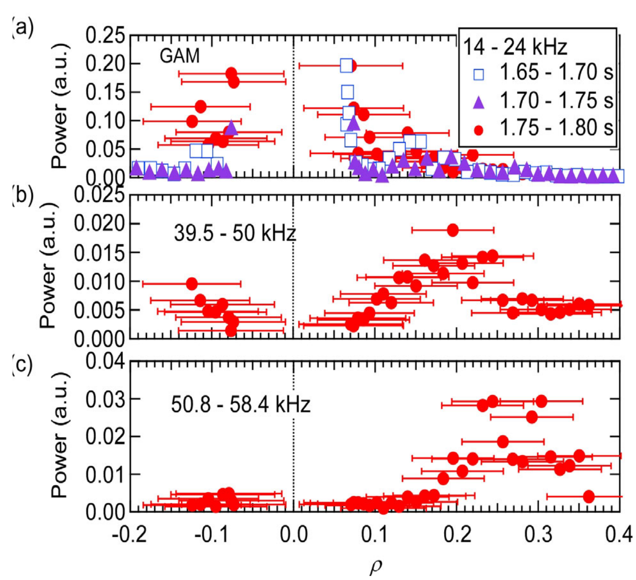

Fig. 5. Spatial distribution of coherent potential fluctuations in each frequency range. The data from 1.75 to 1.80 s are analyzed in Fig. 4.

Summary

An HIBP using a 3-MV tandem accelerator has been installed in LHD and used to measure the electrostatic potential in core plasmas.

The measured potential profile shows the transition from weak negative E_r to strong positive E_r, and the behavior is qualitatively accounted for by neoclassical theory.

From the point of view of the fluctuation measurement, the electrostatic potential fluctuations relating to the RSAE and the energetic particle-induced GAM are measured locally and directly, and their spatial distributions are clarified.

Direct measurement of the potential and its fluctuation by the LHD HIBP will contribute to better understandings of plasma confinement.

Takeshi Ido, Akihiro Shimizu, Masaki Nishiura, Shinji Kato
National Institute for Fusion Science
Toki, Gifu 509-5292, Japan

E-mail: ido@lhd.nifs.ac.jp

References

[1] T. Ido et al., Plasma Fusion Res. **3**, 031 (2008).

[2] A. Shimizu et al., Plasma Fusion Res. (submitted, 2009).

[3] S. Kubo et al., Paper EX/P6-14 presented at the 22nd IAEA Fusion Energy Conference, Geneve, 2008 (http://www-pub.iaea.org/MTCD/Meetings/FEC2008/ex_p6-14.pdf)

[4] K. Toi et al., Paper EX/P8-4 presented at the 22nd IAEA Fusion Energy Conference, Geneve, 2008 (http://www-pub.iaea.org/MTCD/Meetings/FEC2008/ex_p8-4.pdf)

[5] T. Ido et al., Rev. Sci. Instrum. **79**, 10F318 (2008).